Variability of wind wave field by realistic mesoscale and submesoscale eddy field

Gwendal Marechal[1,*] and Charly de Marez[1,*]

[1]Univ. Brest, CNRS, Ifremer, IRD, Laboratoire d'Océanographie Physique et Spatiale, Brest, France
[*]These authors contributed equally to this work.

Correspondence: gwendal.marechal@ifremer.fr

Abstract. Recent altimeters and numerical studies have shown that wind waves interact strongly with small scale open ocean currents, and subsequently modify their amplitude, frequency, and direction. In the present paper we investigate the interactions of wind waves with a large realistic cyclonic eddy. This eddy is subject to instabilities leading to the generation of specific features both at mesoscale and submesoscale. We use the WAVEWATCH III framework to force wind waves in the eddy before and after instabilities occurred. Our findings show that the spatial variability of wave direction frequency and amplitude is very sensitive to the presence of underlying submesoscale structures resulting from the eddy destabilisation. As the surface current vorticity, the intrinsic frequency of incident waves is key in the wave response of the current modulation. Our findings also suggest that surface current gradients can be retrieved thanks to wave height gradients at scale where traditional altimeter measurements fail.

1 Introduction

The ubiquity of mesoscale (10-100 km) and submesoscale (1-10 km) eddies, fronts, and filaments at the superficial layer of the ocean induces a strong variability in the wave field generated by wind: waves-current interactions result in a change of wave height, frequency, and direction (Phillips, 1977; Mei, 1989). From these modulations, it has been proved recently, thanks to both numerical simulations and field measurements, that the effect of currents on waves induces a strong regional inhomogeneity of the wave field (Romero et al., 2017, 2020). In particular, Ardhuin et al. (2017) showed thanks to realistic numerical simulations that the wave height variability is closely linked to surface Kinetic Energy (KE) at mesoscale. Quilfen et al. (2018); Quilfen and Chapron (2019) used high resolution wave height measurements from altimetry to highlight the close link between current gradient and wave height gradient. Villas Bôas and Young (2020) proved in the absence of wave dissipation and wind momentum input that the gradient of the wave direction induced by current is necessarily induced by the solenoidal component of the surface current (vorticity). Finally, Villas Bôas et al. (2020), under the same assumptions, emphasised the narrow link between surface vorticity and the wave height gradient. Besides, surface currents seem to increase the deep-water breaking wave probability (Romero et al., 2017, 2020). The wave breaking at the air-sea interface is the major source of momentum and heat exchange between wave and currents (Cavaleri et al., 2012) or gaz and sea spray production

(Monahan et al., 1986). Surface mesoscale and submesoscale currents, through their interaction with the wind wave field, thus

25 have a significant impact on gas and heat transfers between the ocean and the atmosphere.

In mesoscale surface current field as *e.g.* at boundary currents (Gulf Stream, Agulhas current, Drake passage...) the wave height gradients are mostly due to refraction (change of wave direction, see Irvine and Tilley (1988); Ardhuin et al. (2017); Marechal and Ardhuin (2021)). Indeed mesoscale and submesoscale eddies redistribute spatially the wave action and subsequently generate wave energy convergence and divergence. This explains the strong wave height gradients measured in those

30 current regimes. The same result has also been highlighted for waves propagating in a synthetic current, fully or partially solenoidal, and very turbulent, at scales between $15\,\mathrm{km}$ and $200\,\mathrm{km}$ (White and Fornberg, 1998; Villas Bôas et al., 2020).

In the ocean, the ubiquity of eddies is no longer to be proven (Chelton et al., 2007, 2011; Gula et al., 2015; McWilliams, 2016; Rocha et al., 2016). The interaction between such coherent structures and waves is thus of primary importance for the global distribution of wave properties. In the present study, we analyse the effect of a realistic eddy on the wave properties

35 (amplitude, frequency, and direction). Former similar works already performed such analysis, but only in idealized eddy cases (Gaussian profiles, see Gallet and Young (2014); Mathiesen (1987); White and Fornberg (1998)). However, the structure of eddies in the ocean can strongly differ from textbook analytical idealized profiles (Le Vu et al., 2018; de Marez et al., 2019), such as Gaussian ones, making the study of waves-Gaussian eddy an unrealistic framework. Furthermore, previous studies solely focused on the refraction induced by eddies without discussing the wave height gradients resulting from the interaction

40 (Gallet and Young, 2014; Mathiesen, 1987; White and Fornberg, 1998)). The investigation of wave height variability induced by surface currents is crucial for the anticipation of extreme waves in mesoscale currents (Lavrenov, 1998; Hasselmann et al., 2012), and for remote sensing application where wave height gradients induce a sea states bias (Fu and Glazman, 1991). ?Villas Bôas et al. (2020) showed that wave height gradients and surface current gradients are closely linked, the investigation of how wave height follows the underlying current signal seems to be promising to allow the surface current retrieval without

45 any direct measurements.

The manuscript is organised as follows. In section 2, we introduced the eddy structure used in the study, based on the work of de Marez et al. (2020), and the numerical model built from Ardhuin et al. (2017) without source terms. In section 3, we present the results of the numerical experiments. Finally, in section 4, we discuss on how wave height and current gradient are coupled. Potential perspectives of this present work close this manuscript.

50 ## 2 Method

2.1 The realistic cyclonic eddy

To study the wave propagation through a realistic eddy, we use the outputs of the simulation performed by de Marez et al. (2020). In this study, authors performed spindown idealized simulations, using the Coastal and Regional Ocean COmmunity model, CROCO (Shchepetkin and McWilliams, 2005), that solves the hydrostatic primitive equations (PE) for the velocity

55 $\mathbf{u} = (u, v, w)$, temperature T, and salinity S, using a full equation of state for seawater (Shchepetkin and McWilliams, 2011). Details of the parameterization are fully described in de Marez et al. (2020).

The simulation is initialised with a composite cyclonic eddy as revealed by Argo floats in the northern Arabian Sea (details of the composite extraction are fully described in de Marez et al. (2019)). The eddy is intensified at the surface, but has a deep-reaching influence down to about 1000 m depth. Its initial horizontal shape corresponds to a shielded vorticity monopole:

60   a positive core of vorticity and a shield of negative vorticity (Fig. 1(a)). Its radius, $R = 100$ km, is large compared to the mean regional Rossby radius R_D (47 km, see Chelton et al. (1998)). It is a mesoscale eddy. In the following, mentions to "submesoscale" refer to features and processes occurring at scales that are small compared to R_D (*i.e.* $Bu > 1$).

During the simulation, de Marez et al. (2020) observed that the eddy is unstable with respect to a mixed barotropic/baroclinic instability. The latter deforms the eddy, which eventually evolves into a tripole after about 4 months of simulation. Sharp fronts

65   are subsequently generated in the surface mixed layer at the edge of the tripole. These fronts then become unstable, and this generates submesoscale cyclones and filaments. Near these fronts, diapycnal mixing occurs, causing the potential vorticity to change sign locally, and symmetric instability to develop in the core of the cyclonic eddy. Despite the instabilities, the eddy is not destroyed and remains a large-scale coherent structure for one year of simulation. A full description of instability processes can be found in de Marez et al. (2020). Thus, the final state of the simulation (*i.e.* after about half a year of simulation, see

70   Fig. 1b) represents well a realistic turbulent vorticity field surrounding an eddy in the ocean: the main core of the cyclone is surrounded by filaments and fronts, that lead to sharp vorticity gradients. This vorticity field is far from the usual idealised representation of eddies often considered in the literature, and is closer to reality (see *e.g.* Fig. 1 in Lévy et al. (2018) for an example of a realistic turbulent field above mesoscale eddies).

For the purpose of the present study, we consider the surface velocity fields from the simulation outputs described above.

75   We use the initial state that represents the eddy before instabilities occur (Fig. 1(a)), and the state after 210 days of simulation, in which submesoscale features have been generated by the spontaneous instability of the eddy (Fig. 1(b)).

2.2   The wave model

To describe the dynamics of waves passing through the eddy described above, we use the WAVEWATCH III framework (The WAVEWATCH III ® Development Group, 2016). This model integrates wave action equation

80
$$\partial_t N(\sigma, \theta) + \nabla \cdot (\dot{x} N(\sigma, \theta)) + \partial_k (\dot{k} N(\sigma, \theta)) + \partial_\theta (\dot{\theta} N(\sigma, \theta)) = S, \tag{1}$$

where $N(\sigma, \theta)$ is the wave action ($N(\sigma, \theta) = \frac{E(\sigma, \theta)}{\sigma}$, with $E(\sigma, \theta)$ the two dimensional wave energy spectrum), θ is the wave direction of propagation, $\dot{x}$ is the wave action advection velocity (equal to the sum of the wave group and the surface current vectors), and $\dot{k}$ and $\dot{\theta}$ are the wave advection velocity in the spectral space, their expressions are developed from wave ray equations which describe the wave kinematic (Phillips, 1977; Benetazzo et al., 2013; Ardhuin et al., 2017). The right hand

85   side of Eq. (1) is the sum of the source terms describing the wind energy input, the dissipation due to wave breaking and bottom friction, and the non-linear energy exchange between waves. For this study we consider already well developed waves, propagating in the current field without any source term (no dissipation, no non-linear exchange, and no wind input, *i.e.* $S = 0$).
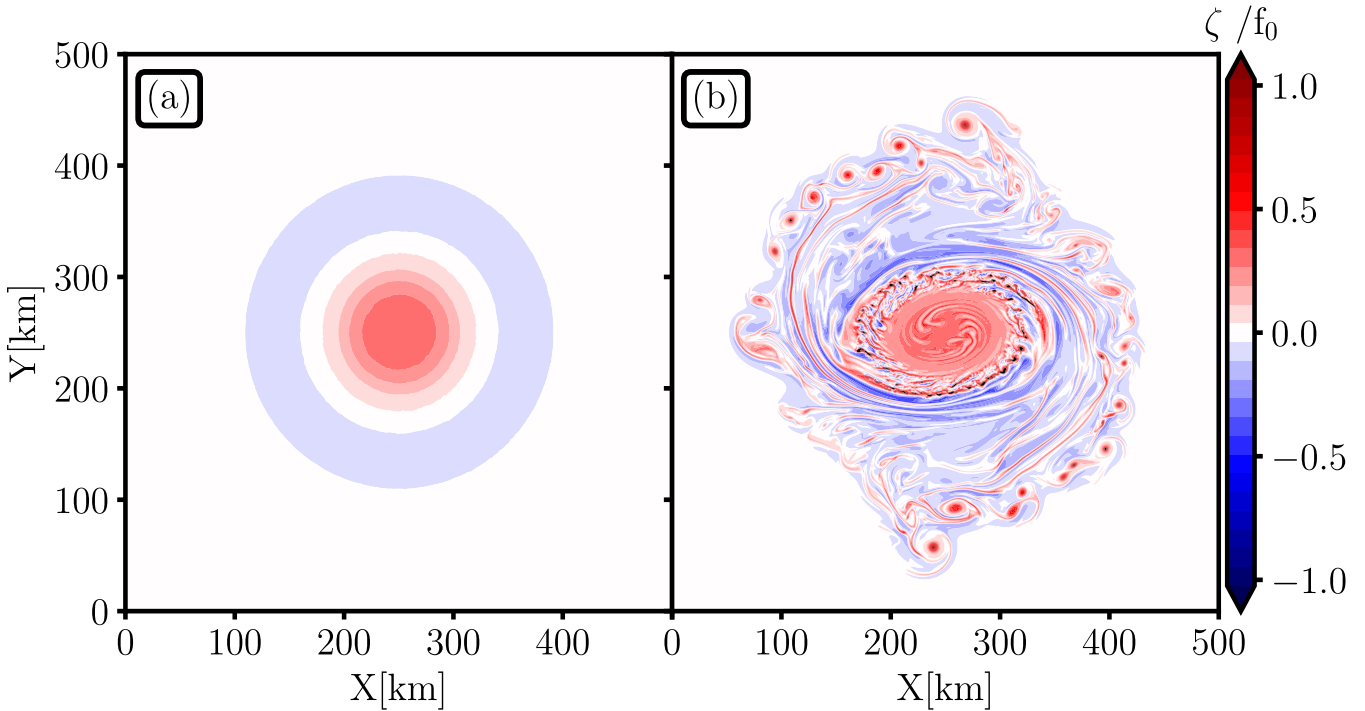
Figure 1. Normalized relative vorticity from de Marez et al. (2020)'s simulation outputs ($f_0 = 5.2\,10^{-5}\,\mathrm{s}^{-1}$ at 23°N) (a) at initialisation and (b) after destabilisation (210 days of simulation), as used in the wave model integration.

In a current field, it is necessary to consider a non-Galilean frame of coordinate (moving frame of reference). The wind waves dispersion relationship is thus impacted because the current induces a Doppler shift of the wave frequency

$$\omega = \sigma + \mathbf{k}.\mathbf{u}, \tag{2}$$

where ω is the absolute frequency, $\mathbf{k}$ the wavenumber vector, σ the intrinsic wave frequency and equal to $\sqrt{gk}$ in deep water (where water depth is largely greater than wave wavelength, here k is a scalar). g is the gravity acceleration and $\mathbf{u}$ is the surface current vector. Bold characters refer to vector notation all along this manuscript.

Throughout this manuscript we discuss the evolution of the significant wave height (H_s) and the mean wave period ($T_{m0,-1}$), known as "bulk" quantities because they are summed over the wave energy spectrum $E(\sigma,\theta)$. They are defined as

$$H_s = 4\sqrt{\iint_{\theta\ \sigma} E(\sigma,\theta)\,d\sigma d\theta}, \tag{3}$$

and

$$T_{m0,-1} = \frac{1}{\int_\theta \int_\sigma E(\sigma,\theta)d\sigma d\theta} \iint_{\theta\ \sigma} \sigma^{-1} E(\sigma,\theta)d\sigma d\theta. \tag{4}$$

The evolution of the wave peak direction (θ_p, θ where $E(\sigma, \theta)$ is maximum) is also studied while waves are travelling in the current field. The performances of the wave model used here have already been discussed in boundary currents systems such as the Gulf Stream, the Agulhas current, or the Drake Passage, especially concerning the H_s estimation (Marechal and Ardhuin, 2021; Ardhuin et al., 2017).

We initialize simulations with waves that are propagating from the west side of a 500×500 km Cartesian domain, with a resolution of 500 m both in meridional and zonal direction. Spectral model is initalized with a narrow band spectrum of frequency spreading on 0.03 Hz, centered at varying peak frequencies f_p=0.1428 Hz, 0.097 Hz, and 0.0602 Hz. The frequencies are chosen to correspond to the mean periods used in the work of Villas Bôas et al. (2020) (7 s, 10.3 s, and 16.6 s). At initialization, $H_s = 1$ m. The wave model global time step is 12 s, the spatial advection time step is 4 s, and the spectral time step is 1 s. The model provide outputs every fifteen minutes. Wave spectra are computed at each grid point, discretized into 48 directions and 32 frequencies. Indeed, dealing with high directional resolution allows a better description of wave refraction, especially in strong rotational current (Ardhuin et al., 2017; Marechal and Ardhuin, 2021).

As mentioned above, surface currents are added in wave propagation simulations. These surface currents are from de Marez et al. (2020)'s simulations output. In one case we considered the initial shape of the cyclonic eddy (Fig. 1(a)). In the other case, we considered the turbulent state of the cyclonic eddy (Fig. 1(b)). In the following, this cases are called the unperturbed and the perturbed cases, respectively. The variation timescale of the current is much longer ($\mathcal{O}(1)$ week) than the wave one (($\mathcal{O}(1)$ minute), thus respecting the steady current assumption. The eddy described in previous section and in de Marez et al. (2020) is an averaged composite eddy reconstructed from measurements in the Arabian Sea (de Marez et al., 2019). The method of reconstruction tends to an underestimation of the eddy intensity. Hence, the intensity of the current has been multiplied by five to increase the potential effects of current on wave properties, while staying geophysicaly realistic (current velocity remains around 2.5 m.s^{-1}). This strategy is comparable to the one presented in Fig. 10 of Gallet and Young (2014).

3 Wave field variability in a cyclonic realistic eddy

The frequency sensibility of the incident waves is studied in both the unperturbed and the perturbed cases.

Waves are dispersive in deep water and are propagating in the current at the group velocity (C_g). T_p=7 s ($T_p= \frac{1}{f_p}$) wave packet is propagating slower than T_p=10.3 s which are propagating slower than T_p=16.6 s waves ($C_g \sim 11$ m.s^{-1}, 16 m.s^{-1} and 26 m.s^{-1} respectively). To reach X=X$_0$ (a given longitude) shorter waves take more time than longer waves. The snapshots presented in Figs. 2, 3, and 4 are thus taken for three different time outputs depending on T_p of the incident waves (t=105 s, 90 s and 75 s respectively). Surface currents modulate amplitude, frequency and waves direction, the variability of those quantities are highlighted through H_s, $T_{m0,-1}$, and θ_p fields. The respond of other waves parameters for a prescribed underlying current, as the directional spreading or the mean direction, are not described in this manuscript.
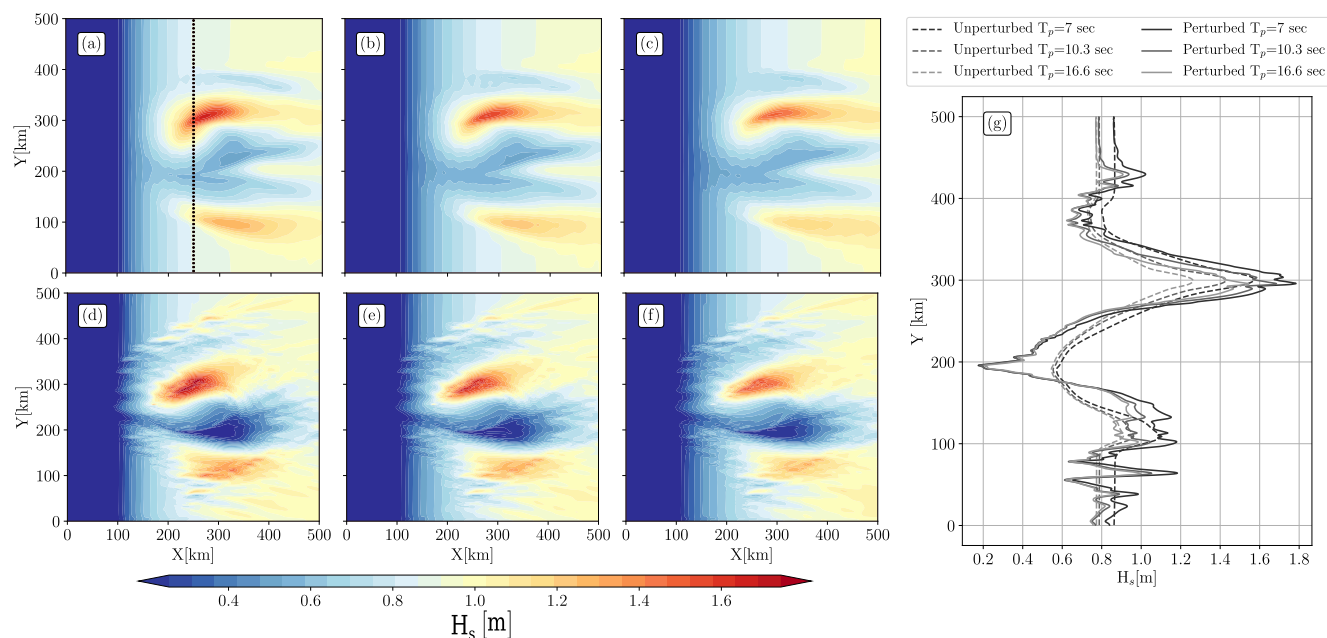
Figure 2. Instantaneous significant wave height field for (a,d) T_p=7 s, (b,e) 10.3 s, and (c,f) 16.6 s incident waves. The initial wave field is initialized at H_s=1 m. The first line (a,b,c) shows instantaneous field for simulations forced with the unperturbed eddy (Fig. 1(a)); the second line (d,e,f) shows the same instantaneous field but for simulations forced with the perturbed eddy (Fig1(b)). Panel (g) shows significant wave height along X = 250 km (dashed line in panel (a)) for all simulations.

3.1 Modulation of wave parameters

130 **3.1.1 Significant wave height**

Surface currents induce a strong regional H_s variability, specially in a highly solenoidal field (Marechal and Ardhuin, 2021).

Wave train is propagating from the west boundary with an initial direction of 270° (0° is the geographical North, and the direction convention is where waves are propagating). Outputs of wave simulation performed in the unperturbed and perturbed eddy is given in Fig. 2. The presence of an underlying vortex induce a strong wave height gradient (∇H_s), inside and outside

135 the eddy. Model forced with the unperturbed eddy (2a,b,c) shows coherent alternate sign H_s structures along meridians (fixed X−axis). An important lens shape dipole of H_s enhancement and decrease is noticeable in the field. H_s reaches a maximum of 1.6 m, 1.4 m, 1.2 m (60, 40, 20 % enhancement with respect to the initial H_s) at X =250 km , Y= 300 km for simulations initialized with T_p = 7, 10.3 and 16.6 s respectively (Fig. 2g). A secondary H_s maximum is apparent at the southernmost part of the domain (enhancement of ∼ 20%) at X =300 km , Y= 75 km. The enhanced H_s areas are associated to the boundary of the

140 inner eddy core ($\zeta > 0$) and the vorticity ring ($\zeta < 0$) that surround the principal structure. Decrease of H_s is also apparent in the field, specially in the core of the eddy (∼ -40% decrease with respect to the initial H_s) with a scattering of the signal easterly of X=300 km within Y=[150,300] km in two large tongues. The decrease of H_s at X=250 km are identical for simulations

forced with the unperturbed eddy (Fig. 2g) for each wave model's initialization. Globally where waves are propagating against the current, H_s is enhanced which agree with waves-eddies interactions simulated in realistic fields ; (see Fig. 6 of Romero

145 et al. (2020) and Fig.1 of Ardhuin et al. (2017)).

Model forced with perturbed eddy shows stronger spatial inhomogeneity in the wave field (Fig. 2d,e,f). As simulations forced with the unperturbed eddy (2a,b,c), the H_s field is matching pretty well with the current forcing used (Fig. 1b). H_s is mostly modulated by the center structure of the perturbed eddy. Nevertheless, significant ∇H_s are occurring in the submesoscale eddies that have been emerged spontaneously all around the center structure explicitly shown in Fig. 2g at Y<180 km and Y>

150 350 km. Wave actions in the perturbed eddy is more scattered (mostly zonally due to the initial direction of the incident wave packet) than in the unperturbed eddy. Wave height is also larger at X=250 km, Y=300 km and smaller at X=300 km, Y=200 km than in perturbed eddy simulations. ∇H_s is globally the strongest for simulations initialized with T_p=7 s wave packet (Fig. 2a,d,g) than in simulations with T_p=10.3 s and T_p=16.6 s.

3.1.2 Peak direction

155 The refraction induced by the surface currents can be captured at the first order by the θ_p field. Waves are turning in the current field due to refraction, globally toward the South (θ_p decreases) in the bottom part of the domain and toward the North (θ_p increases) in the upper part.

When waves pass through the eddy, θ_p changes due to the vorticity field, at X= 125 km for the unperturbed eddy (Fig.3a,b,c), slightly upwind for the perturbed eddy; at X= 90 km (Fig.3d,e,f). Patterns showed in Fig. 3 are similar to the H_s gradient

160 showed in Fig. 2 with a large scale dipole for simulation forced with unperturbed eddy and both a large scale and small scale signal gradient for simulations forced with the perturbed eddy. The large yellow bands in the left part of each panels are spurious.

The peak direction gradient ($\nabla \theta_p$) intensity is function of both the incident wave frequency and the underlying vorticity field (Dysthe, 2001; Kenyon, 1971). $\nabla \theta_p$ is stronger for simulations initialized with T_p=7 s (Fig. 3a,d) than for simulations initialized

165 with T_p=10.3 s and 16.6 s. In the same way, $\nabla \theta_p$ is enhanced for simulations forced with perturbed eddy (Fig. 3d,e,f)) where current field is more turbulent. This result corroborates Villas Bôas et al. (2020)'s findings where authors forced wave model with synthetic surface current inverted from KE spectrum (with a random phase). The more the current was turbulent, the more waves scattered with convergence and divergence areas of wave trajectories, like a random walk. These areas of convergence and divergence of waves trajectory are discussed later in this manuscript. In the presence of current, waves follow the Fermat

170 principle, in the geometric optic framework waves take the shortest path to join two distant areas. For linear waves in deep water the curvature of wave ray is proportional to $\frac{\zeta}{C_g}$, with ζ the current vorticity and C_g the wave group velocity.

Villas Bôas and Young (2020) demonstrated that in the absence of forcing and dissipation, waves are scattered by the rotationnal components of the current. The current field used as model forcing is highly rotational (de Marez et al., 2020).

3.1.3 Mean wave period

175 Wave simulations are initialized with different wave train peak frequencies, thus impacting values of $T_{m0,-1}$.
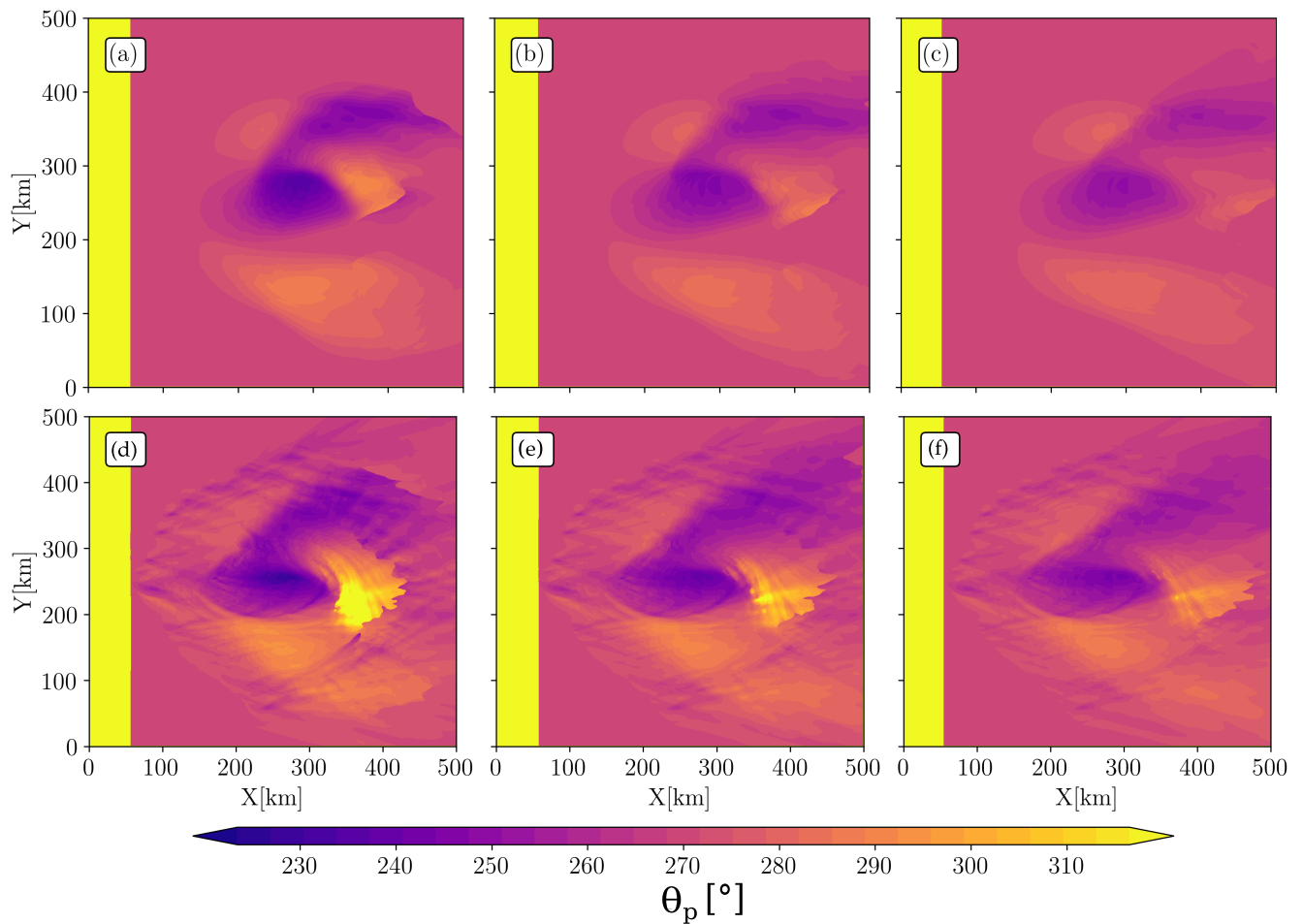
Figure 3. Instantaneous peak direction (θ_p) for (a,d) T_p=7 s, (b,e) 10.3 s, and (c,f) 16.6 s incident waves. The initial wave direction, at X=0 is θ_p=270°. The first line (a,b,c) shows instantaneous field for simulations forced with the unperturbed eddy (Fig. 1(a)); the second line (d,e,f) shows the same instantaneous field but for simulations forced with the perturbed eddy (Fig. 1(b)).)
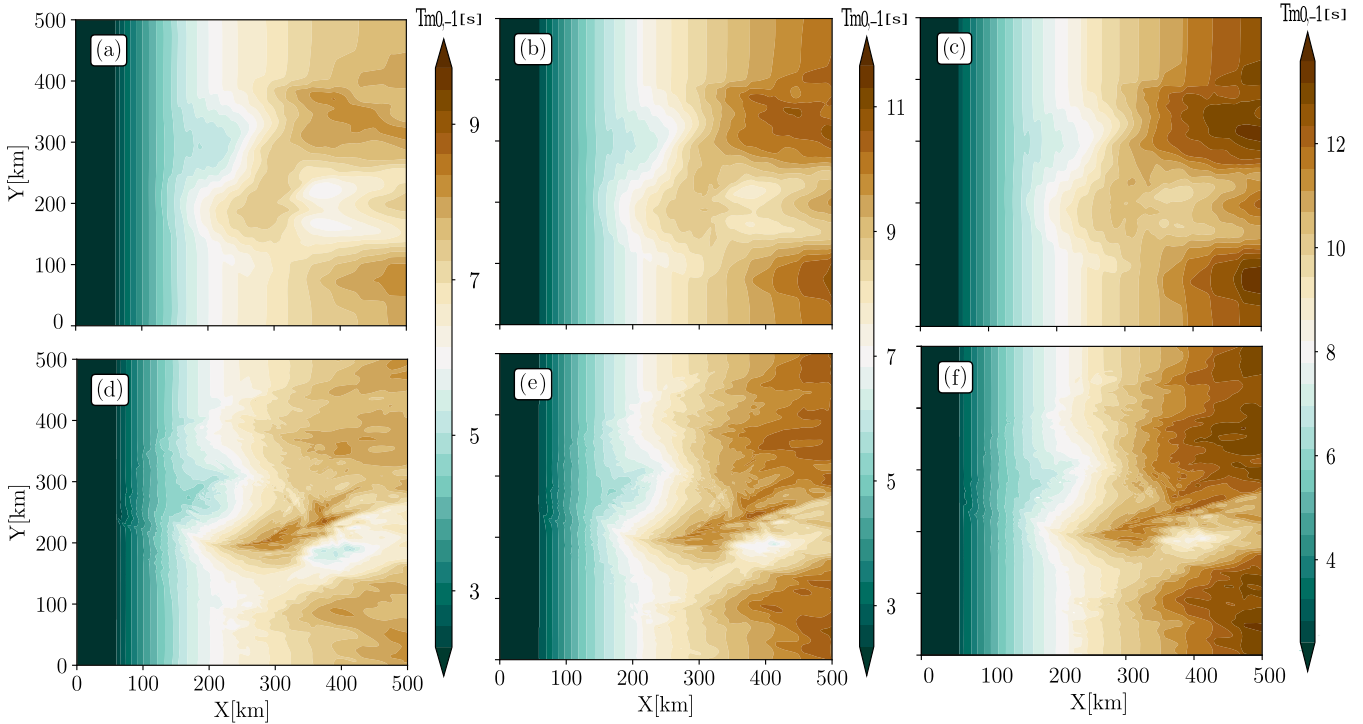
Figure 4. Instantaneous mean period ($T_{m0,-1}$) for (a,d) T_p=7 s, (b,e) 10.3 s, and (c,f) 16.6 s incident waves. The first line (a,b,c) shows instantaneous field for simulations forced with the unperturbed eddy (Fig.1(a)); the second line (d,e,f) shows the same instantaneous field but for simulations forced with the perturbed eddy (Fig.1(b)). Note that colorbars have different scales for each values of T_p

At first glance, the spatial inhomogeneity is more striking for simulation forced with the perturbed eddy, similarly as for the H_s instantaneous fields (Fig. 2).

As waves are dispersive, longer waves are faster than short ones resulting in a large scale zonal gradient of $T_{m0,-1}$. Qualitatively, waves are globally shorter (smaller $T_{m0,-1}$) where H_s is enhanced (Fig. 2). This is mostly the case where current is in
180 the opposite direction than the wave propagation direction. Indeed, as currents induce a Doppler shift on the wave frequency Eq.(2), where waves and current are opposite, waves are shortened due to the conservation of wave action ($D_t N = 0$, Eq. (1)). Waves and currents also exchange their energy by conservation of absolute frequency. We precise that the change of H_s induced by current is due to a superposition of processes as explicitly described in Ardhuin et al. (2017); Quilfen et al. (2018); Kudryavtsev et al. (2017b) and all along this manuscript.
185 Finally we guess that in a fully diverging current, $T_{m0,-1}$ field would be more impacted, as described in Villas Bôas et al. (2020). The waves stripes induced by refraction (Fig. 3) is also captured in the mean wave period signal and more noticeable in the perturbed eddy (Fig. 4d,e,f) than in the unperturbed case (Fig. 4a,b,c).

3.2 Ray tracing

In a rotational current field, wave rays are curved because of refraction. In a current field the wave elevation variance (or energy)
190 ($E(\sigma,\theta)$) is not conserved, waves and current exchange their own energy, nevertheless wave action ($\frac{E(\sigma,\theta)}{\sigma}$) is conserved. It
is possible to follow the path along which wave action is conserved thanks to a Monte-Carlo ray tracing (Spencer and Murty,
1962). Refraction seems to be the main process that induce a change of H$_s$ at mesoscale and submesoscale (Irvine and Tilley,
1988; Ardhuin et al., 2017; Romero et al., 2020; Marechal and Ardhuin, 2021).

In a isolated vortex as described in the present study, current-induced refraction results in a strong wave field inhomogeneity
195 (Fig. 2). In the absence of wind and dissipation in a stationary framework, for $\frac{C_g}{u} = \epsilon$ (with $\epsilon \ll 1$), wave refraction can be
described through ray equation:

$$\mathbf{C}_g.\boldsymbol{\nabla}\theta = -\frac{1}{k}\mathbf{n}.\boldsymbol{\nabla}(\mathbf{k}.\mathbf{u}), \tag{5}$$

Refraction is all the more important where waves and currents vectors are perpendicular, given by $\mathbf{n}.\boldsymbol{\nabla}$ term in Eq. (5). In
the framework of a monochromatic waves ($\lim_{\sigma \to \sigma_0} E(\sigma)$) and for a prescribed incident direction, refraction can be capture
200 by a Monte-Carlo ray tracing method. In a real ocean, wave field is a superposition of wave train with specific direction and
frequency, thus ray tracing is only an approximation of the wave kinematic.

Examples of ray-tracing are shown in Fig. 5 in both unperturbed and perturbed eddy cases. The initialized direction is 270°
(waves are coming from the west boundary) and initial frequencies are the same than the ones discussed above (T$_p$ =7 s, 10.3
s, and 16.6 s peak periods). The refraction induced by the surface current is sensitive to both the underlying current and the
205 frequency (or wavelength) of the incident waves. Indeed, the radius of curvature of waves rays is larger where the current field
is highly rotational (Fig. 5d,e,f) and when simulations are forced with T$_p$=7 s waves (Fig. 5a,d) (confirmed by theoretical works
performed by Kenyon (1971) or Dysthe (2001)).

In the unperturbed eddy case, the wave train is refracted both by the eddy's edge (toward the South) and the central part
of the eddy (toward the North) (Fig. 5a,b,c). This leads to two wave rays focalisation areas (Fig. 5a,b,c). These focalisation
210 areas are slightly shifted zonally toward the east when the incident wave frequency increases. The number of focalisation areas
increases in the perturbed eddy with a maximum of convergence zones for T$_p$= 7 s incident waves, shown in Fig. 5d. One can
notice that rays convergent areas are localised where H$_s$ reaches peaks (Fig. 2), specially at the edge of the positive vorticity
core. The strong vorticity field both for unperturbed and perturbed cyclonic eddy induces a wave rays scattering which can
reach a deviation of several hundred kilometers with respect to a propagation without background current specially for short
215 waves incidence (Fig. 5a,d). These strong scattering can be responsible of the the space-time bias in the waves arrival on the
coast forecasts described by Gallet and Young (2014) or Smit and Janssen (2019).

This ray tracing study highlights the non local effect of current on wave refraction: focalisation can occur even where the
surface current is null, thus resulting in wave height enhancement both inside and outside the eddy.
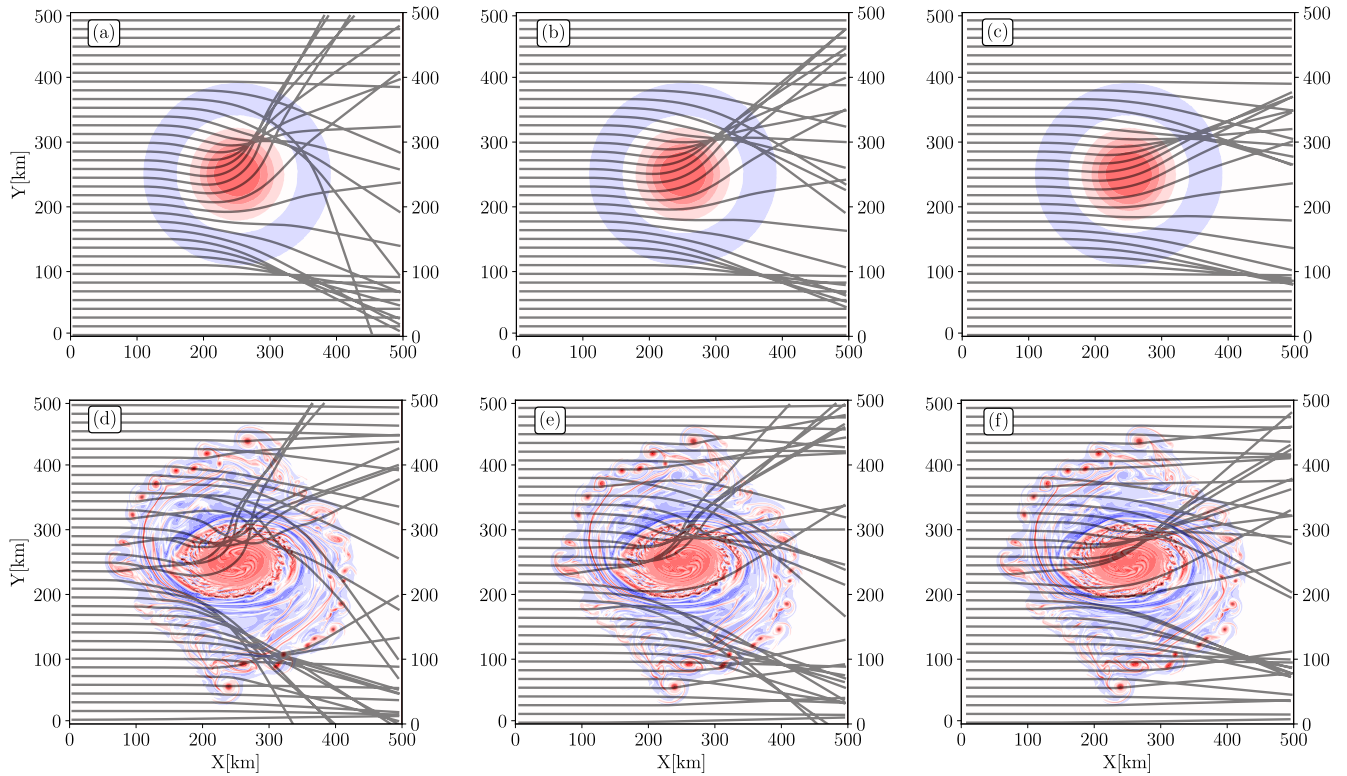
Figure 5. (a,b,c) Ray tracing for waves travelling over an unperturbed eddy with T_p =7 s, (a) 10.3 s (b), and 16.6 s (c) peak period. (d,e,f) same but for waves travelling over a perturbed eddy. Background color shows the surface vorticity, with the same colorscale of Fig 1

4 Is it possible to reconstruct surface current gradients *via* the measurement of the wave height gradient?

220   Surface current gradient module ($\nabla U = \sqrt{\partial_x U^2 + \partial_y U^2}$, $U = \sqrt{u^2 + v^2}$) and especially vorticity (ζ) induce a strong wave height gradient (∇H_s)(Villas Bôas et al., 2020; Romero et al., 2020; Marechal and Ardhuin, 2021). Note that both ∇U and ∇H_s are scalars. Assuming Wentzel–Kramers–Brillouin (WKB) approximation and that waves are generated from a remote storm (no local wind) without breaking, ∇U can be written with respect to ∇H_s (6) such as

$$\frac{\nabla H_s \sigma}{(kH_s)} \sim \nabla U \tag{6}$$

225   ∇H_s is thus function both of surface current gradient and wave steepness (kH_s). The full development is given in Appendix 1. Right and left hand sides of Eq. (6) are shown in Fig. 6 in the perturbed eddy case, for incident waves at T_p=7 s. Both ∇H_s and ∇U have been projected along and perpendicular to the wave peak direction respectively. Both terms of Eq. (6) are of the same order of magnitude with values slightly higher for the $\frac{\nabla H_s \sigma}{(kH_s)}$ field (Fig. 6b). ∇U shows rounded structures (Fig. 6a) whereas ∇H_s field shows more elongated-horizontal, typical structures of current-induced refraction (Villas Bôas et al., 2020; de Souza
230   et al., 2021). Nevertheless, both fields are matching both at mesoscale (the central eddy) and at smaller scale (submesoscale
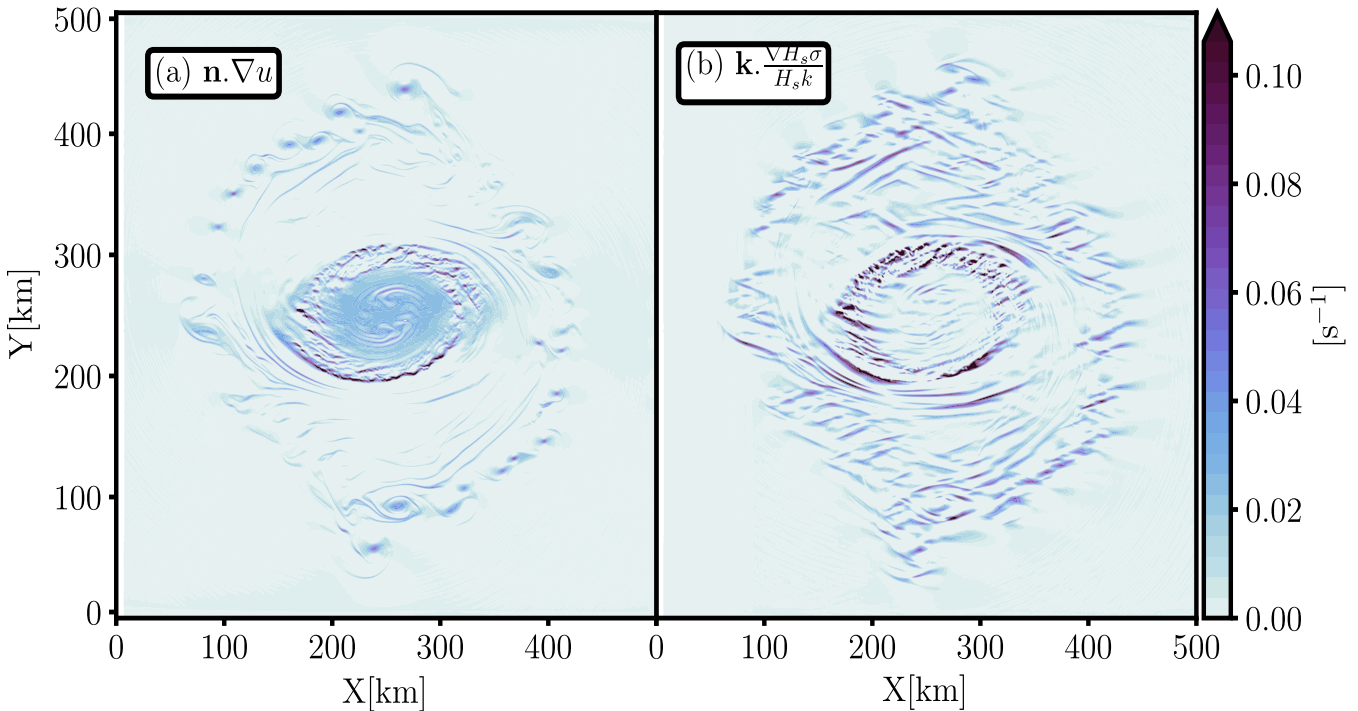
Figure 6. (a) Surface current gradient (∇u) projected perpendicular to the peak wave direction vector, *i.e.* the right hand side of Eq. (6) and (b) normalized wave height gradient ($\frac{\nabla H_s \sigma}{H_s k}$) projected in the peak wave direction vector, *i.e.* the left hand side of Eq. (6), both for the perturbed eddy case. This instantaneous field is for simulation initialized with $T_p = 7$ s.

eddies around the principal ellipsoidal eddy). ∇U exhibits fronts at the boundary of the central eddy also captured by the normalized ∇H_s field. Inside the central ellipsoidal eddy, ∇U shows a quite smooth and homogeneous field (Fig. 6a) whereas Fig. 6b presents ∇H_s stripes. The analysis of Fig. 6b shows that the wave model captures surface currents gradient, without any information on surface current. The sensibility of wave field gradient to the spectral width (σ_f) of the incident wave packet have been tested, the results shown in Fig. 6b are not affected by this modification in the wave model.

Where oceanic eddy became unstable spontaneously due to horizontal sheared current structures (barotropic instabilities) or vertical buoyancy gradient (baroclinic instabilities, mixed layer instabilities), the resulting ocean surface provide specific ∇U features. Certain of these structures are well captured by the normalized ∇H_s field. Oceanic meso- and submesoscale instabilities can induce mixing, vertical movements or water masses trapping which could be now approached only thanks to an investigation of ∇H_s field. Regional ∇H_s field are possibly recoverable at very high resolution thanks to remote sensing imagery as optical techniques (Kudryavtsev et al., 2017a).

These results point out the promising opportunities to invert wave gradient properties to retrieve the underlying surface current gradient at high resolution, specially at scales where altimeters are unable to reconstruct.

Measuring surface currents from space is a very challenging purpose since past decades (Villas Bôas et al., 2019). Altimetry

245 has proved its robustness to retrieve surface current by measuring the dynamical ocean height at a resolution of several hundred kilometers (Rio et al., 2014; Ballarotta et al., 2019). The benefits of this method is mainly the global coverage of the ocean surface in a dozen of days by combining several altimeters missions. Nevertheless, although altimeters sample ocean surface every $\sim 10\,\mathrm{km}$, the accumulation of noise along altimeter track induces a loss of resolution in the surface current retrieval. Even if mesoscale eddies are observable from space (Chelton et al., 2011), surface dynamics at smaller scales are drawn in the noise

250 signal. This reality has highlighted the necessity to measure surface currents at higher resolution triggering the emergence of new satellite missions based on innovative measurements method (Ardhuin et al., 2018; Morrow et al., 2019; Ardhuin et al., 2021). In term of wave-current interactions, as current affects waves principally at scales smaller than $200\,\mathrm{km}$ (Ardhuin et al., 2017; Villas Bôas et al., 2020), waves models forced with currents derived from altimetry do not reproduce realistic ∇H_s (Marechal and Ardhuin, 2021) or wave breaking statistic (Romero et al., 2017, 2020). This is all the more true in boundary

255 currents where mesoscale and submesoscale are ubiquitous (Rocha et al., 2016; Mensa et al., 2013). The small scale dynamic present in the perturbed eddy field used in this study is not captured by potential altimeter measurements (see discussion in de Marez et al. (2020)).

In this study, we showed that a realistic eddy field induces inhomogeneities in the wave field at all scales from a few to hundreds of kilometers. Recent works have shown that small scale wave height variabilities can be captured using filtered

260 altimeter data (Quilfen and Chapron, 2019; Dodet et al., 2020; Marechal and Ardhuin, 2021) or optical remote sensing images (Kudryavtsev et al., 2017b). However, surface currents retrieval from SSH measurements is very limited in term of effective resolution. In our case, the eddy presented in Fig. 1 cannot be monitored from space by the use of traditional altimeters and thus even less the different oceanic processes that occur inside the vortex de Marez et al. (2019). Here, knowing both the spatial significant wave height gradient and the wavelength of the incident waves, the existence (or not) of such perturbed eddy can be

265 monitored from remote sensing measurements and perhaps that the different oceanic processes that occur in the vortex could be approached through specific wave height gradient features observations.

5 Conclusion and perspectives

A new study of wave-current interactions have been investigated in a highly rotational isolated vortex. Waves have been simulated by the use of a third generation phase averaged spectral model initialized with wave spectra centered at different

270 frequency ($T_p =7$, 10.3, and 16.6 s). Although wave scattering by an oceanic vortex has already been studied in the past (Mathiesen, 1987; White and Fornberg, 1998; Gallet and Young, 2014), this study completes studies performed in the past with *(1)* a description of the evolution of the wave bulk parameters as wave height and mean wave period inside and outside the isolated vortex, and *(2)* the investigation of how a realistic and perturbed eddy (that really occur in a real ocean) induces variability in the wave field. Both wave dynamics and kinematics are changed by the presence of an underlying current. These

275 changes are all the more pronounced when incident waves are shorts and where the underlying current is highly energetic within a large band of scales. Under the WKB approximation and in the geometric theory framework, the significant wave

height gradient field normalized by wave frequency of the incident waves has been described as a function of the surface current gradient. Besides a good coherence in order of magnitude between the two quantities, structures of significant wave height gradient are very sensitive to the underlying surface current. Measurements of sea surface height from space are able

280 to monitoring surface currents at global scale until several hundreds kilometers in a ice-free areas. All the surface dynamic at smaller scales cannot be retrieved by the used of a constellations of traditional altimeters whereas a lot of oceanic processes occur at those scales (from 1-100 km). This manuscript have shown the possibility to invert the inhomogeneity in the waves field to retrieved surface current gradients and thus approach the small scale processes (vertical movements, mixing, shear flows...) without measurement of surface currents.

285 Finally, investigations of fully couple simulations (atmosphere-waves-ocean) could be performed to investigate how the realistic vortex is modified by the wave-induced Stokes drift or how potential breaking events induce by the current modify the air entrainment and thus the turbulence in the atmospheric boundary layers.

Data availability. The cyclonic vortex field is available at https://data.mendeley.com/datasets/bwkctkk5bn/1.

References

290 Ardhuin, F., Rascle, N., Chapron, B., Gula, J., Molemaker, J., Gille, S. T., Menemenlis, D., and Rocha, C.: Small scale currents have large effects on wind wave heights, J. Geophys. Res., 122, 4500–4517, https://doi.org/10.1002/2016JC012413, 2017.

Ardhuin, F., Aksenov, Y., Benetazzo, A., Bertino, L., Brandt, P., Caubet, E., Chapron, B., Collard, F., Cravatte, S., Dias, F., Dibarboure, G., Gaultier, L., Johannessen, J., Korosov, A., Manucharyan, G., Menemenlis, D., Menendez, M., Monnier, G., Mouche, A., Nouguier, F., Nurser, G., Rampal, P., Reniers, A., Rodriguez, E., Stopa, J., Tison, C., Tissier, M., Ubelmann, C., van Sebille, E., Vialard, J., and Xie, J.:

295 Measuring currents, ice drift, and waves from space: the Sea Surface KInematics Multiscale monitoring (SKIM) concept, Ocean Sci., 14, 337–354, https://doi.org/10.5194/os-2017-65, 2018.

Ardhuin, F., Alday Gonzalez, M. F., and Yurovskaya, M.: Total Surface Current Vector and Shear from a Sequence of Satellite images: Effect of Waves in Opposite Directions, Earth and Space Science Open Archive, 2021.

Ballarotta, M., Ubelmann, C., Pujol, M.-I., Taburet, G., Fournier, F., Legeais, J.-F., Faugere, Y., Delepoulle, A., Chelton, D., Dibarboure, G.,

300 and Picot, N.: On the resolutions of ocean altimetry maps, Ocean Science Discussions, https://doi.org/10.5194/os-2018-156, 2019.

Benetazzo, A., Carniel, S., Sclavo, M., and Bergamasco, A.: Wave–current interaction: Effect on the wave field in a semi-enclosed basin, Ocean Modelling, 70, 152–165, 2013.

Cavaleri, L., Fox-Kemper, B., and Hemer, M.: Wind Waves in the Coupled Climate System, Bull. Amer. Meteorol. Soc., 78, 1651–1661, 2012.

305 Chelton, D. B., deSzoeke, R. A., Schlax, M. G., El Naggar, K., and Siwertz, N.: Geographical Variability of the First Baroclinic Rossby Radius of Deformation, Journal of Physical Oceanography, 28, 433–460, https://doi.org/10.1175/1520-0485(1998)028<0433:GVOTFB>2.0.CO;2, 1998.

Chelton, D. B., Schlax, M. G., Samelson, R. M., and de Szoeke, R. A.: Global observations of large oceanic eddies, Geophysical Research Letters, 34, https://doi.org/10.1029/2007GL030812, 2007.

310 Chelton, D. B., Schlax, M. G., and Samelson, R. M.: Global observations of nonlinear mesoscale eddies, Progress in Oceanography, 91, 167–216, https://doi.org/10.1016/j.pocean.2011.01.002, 2011.

de Marez, C., L'Hégaret, P., Morvan, M., and Carton, X.: On the 3D structure of eddies in the Arabian Sea, Deep Sea Research Part I: Oceanographic Research Papers, 150, 103 057, https://doi.org/10.1016/j.dsr.2019.06.003, 2019.

de Marez, C., Meunier, T., Morvan, M., L'Hégaret, P., and Carton, X.: Study of the stability of a large realistic cyclonic eddy, Ocean

315 Modelling, 146, 101 540, https://doi.org/10.1016/j.ocemod.2019.101540, 2020.

de Souza, J. M. A. C., Couto, P., Soutelino, R., and Roughan, M.: Evaluation of four global ocean reanalysis products for New Zealand waters–A guide for regional ocean modelling, New Zealand Journal of Marine and Freshwater Research, 55, 132–155, 2021.

Dodet, G., Piolle, J.-F., Quilfen, Y., Abdalla, S., Accensi, M., Ardhuin, F., Ash, E., Bidlot, J.-R., Gommenginger, C., Marechal, G., Passaro, M., Quartly, G., Stopa, J., Timmermans, B., Young, I., Cipollini, P., and Donlon, C.: The Sea State CCI dataset v1: towards a sea state

320 climate data record based on satellite observations, Earth System Sci. Data, 12, 1929–1951, https://doi.org/10.5194/essd-12-1929-2020, 2020.

Dysthe, K. B.: Refraction of gravity waves by weak current gradients, J. Fluid Mech., 442, 157–159, 2001.

Fu, L.-L. and Glazman, R.: The effect of the degree of wave development on the sea state bias in radar altimetry measurement, Journal of Geophysical Research: Oceans, 96, 829–834, 1991.

325 Gallet, B. and Young, W. R.: Refraction of swell by surface currents, J. Mar. Res., 72, 105–126, https://doi.org/10.1357/002224014813758959, 2014.

Gula, J., Molemaker, M. J., and Mcwilliams, J. C.: Gulf Stream Dynamics along the Southeastern U.S. Seaboard, J. Phys. Oceanogr., 45, 690–715, 2015.

Hasselmann, K., Chapron, B., Aouf, L., Ardhuin, F., Collard, F., Engen, G., Hasselmann, S., Heimbach, P., Janssen, P., Johnsen, H., Krogstad,
330 H., Lehner, S., Li, J.-G., Li, X.-M., Rosenthal, W., and Schulz-Stellenfleth, J.: The ERS SAR Wave Mode: a breakthrough in global ocean wave observations, in: ERS Missions: 20 Years of Observing Earth, pp. 165–198, European Space Agency, Noordwijk, The Netherlands, 2012.

Irvine, D. E. and Tilley, D. G.: Ocean wave directional spectra and wave-current interaction in the Agulhas from the shuttle imaging radar-B synthetic aperture radar, J. Geophys. Res., 93, 15 389–15 401, 1988.

335 Kenyon, K. E.: Wave refraction in Ocean Current, Deep-Sea Res., 18, 1971.

Kudryavtsev, V., Yurovskaya, M., Chapron, B., Collard, F., and Donlon, C.: Sun glitter Imagery of Surface Waves. Part 1: Directional spectrum retrieval and validation, J. Geophys. Res., 122, https://doi.org/10.1002/2016JC012425, 2017a.

Kudryavtsev, V., Yurovskaya, M., Chapron, B., Collard, F., and Donlon, C.: Sun glitter Imagery of Surface Waves. Part 2: Waves Transformation on Ocean Currents, J. Geophys. Res., 122, https://doi.org/10.1002/2016JC012426, 2017b.

340 Lavrenov, I.: The wave energy concentration at the Agulhas current off South Africa, Natural hazards, 17, 117–127, 1998.

Le Vu, B., Stegner, A., and Arsouze, T.: Angular Momentum Eddy Detection and Tracking Algorithm (AMEDA) and Its Application to Coastal Eddy Formation, Journal of Atmospheric and Oceanic Technology, 35, 739–762, https://doi.org/10.1175/JTECH-D-17-0010.1, 2018.

Lévy, M., Franks, P. J. S., and Smith, K. S.: The role of submesoscale currents in structuring marine ecosystems, Nature Communications,
345 9, 4758, https://doi.org/10.1038/s41467-018-07059-3, 2018.

Marechal, G. and Ardhuin, F.: Surface Currents and Significant Wave Height Gradients: Matching Numerical Models and High-Resolution Altimeter Wave Heights in the Agulhas Current Region, Journal of Geophysical Research: Oceans, 126, e2020JC016 564, 2021.

Mathiesen, M.: Wave refraction by a current whirl, J. Geophys. Res., 92, 3905–3912, 1987.

McWilliams, J. C.: Submesoscale currents in the ocean, 427, 20160 117, https://doi.org/10.1098/rspa.2016.0117, 2016.

350 Mei, C. C.: Applied dynamics of ocean surface waves, World Scientific, Singapore, second edn., 740 p., 1989.

Mensa, J. A., Garraffo, Z., Griffa, A., Özgökmen, T. M., Haza, A., and Veneziani, M.: Seasonality of the submesoscale dynamics in the Gulf Stream region, Ocean Dynamics, 63, 923–941, 2013.

Monahan, E. C., Spiel, D. E., and Davidson, K. L.: A model of marine aerosol generation via whitecaps and wave disruption, in: Oceanic whitecaps, pp. 167–174, Springer, 1986.

355 Morrow, R., Fu, L.-L., Ardhuin, F., Benkiran, M., Chapron, B., Cosme, E., D?Ovidio, F., Farrar, J. T., Gille, S. T., Lapeyre, G., Traon, P.-Y. L., Pascual, A., Ponte, A., Qiu, B., Rascle, N., Ubelmann, C., Wang, J., and Zaron, E. D.: Global observations of fine-scale ocean surface topography with the Surface Water and Ocean Topography (SWOT) Mission, 6, 232, https://doi.org/10.3389/fmars.2019.00232, 2019.

Phillips, O. M.: The dynamics of the upper ocean, Cambridge University Press, London, 336 p., 1977.

Quilfen, Y. and Chapron, B.: Ocean Surface Wave-Current Signatures From Satellite Altimeter Measurements, Geophys. Res. Lett., 216,
360 253–261, https://doi.org/10.1029/2018GL081029, 2019.

Quilfen, Y., Yurovskaya, M., Chapron, B., and Ardhuin, F.: Storm waves sharpening in the Agulhas current: satellite observations and modeling, Remote Sens. Environ., 216, 561–571, https://doi.org/10.1016/j.rse.2018.07.020, 2018.

Rio, M.-H., Mulet, S., and Picot, N.: Beyond GOCE for the ocean circulation estimate: Synergetic use of altimetry, gravimetry, and in situ data provides new insight into geostrophic and Ekman currents, Geophys. Res. Lett., 41, 8918–8925, https://doi.org/10.1002/2014GL061773, 2014.

Rocha, C. B., Chereskin, T. K., and Gille, S. T.: Mesoscale to Submesoscale Wavenumber Spectra in Drake Passage, J. Phys. Oceanogr., 46, 601–620, https://doi.org/10.1175/JPO-D-15-0087.1, 2016.

Romero, L., Lenain, L., and Melville, W. K.: Observations of Surface Wave–Current Interaction, J. Phys. Oceanogr., 47, 615–632, https://doi.org/10.1175/JPO-D-16-0108.1, 2017.

Romero, L., Hypolite, D., and McWilliams, J. C.: Submesoscale current effects on surface waves, Ocean Modelling, 153, 101 662, 2020.

Shchepetkin, A. F. and McWilliams, J. C.: The regional oceanic modeling system (ROMS): a split-explicit, free-surface, topography-following-coordinate oceanic model, Ocean Modelling, 9, 347–404, https://doi.org/10.1016/j.ocemod.2004.08.002, 2005.

Shchepetkin, A. F. and McWilliams, J. C.: Accurate Boussinesq oceanic modeling with a practical, "Stiffened" Equation of State, Ocean Modelling, 38, 41–70, https://doi.org/10.1016/j.ocemod.2011.01.010, 2011.

Smit, P. B. and Janssen, T. T.: Swell propagation through submesoscale turbulence, Journal of Physical Oceanography, 49, 2615–2630, 2019.

Spencer, G. and Murty, M.: General ray-tracing procedure, JOSA, 52, 672–678, 1962.

The WAVEWATCH III® Development Group: User manual and system documentation of WAVEWATCH III® version 5.16, Tech. Note 329, NOAA/NWS/NCEP/MMAB, College Park, MD, USA, 326 pp. + Appendices, 2016.

Villas Bôas, A. B. and Young, W. R.: Integrated observations and modeling of winds, currents, and waves: requirements and challenges for the next decade, J. Fluid Mech., 890, R3, https://doi.org/10.1017/jfm.2020.116, 2020.

Villas Bôas, A. B., Ardhuin, F., Gommenginger, C., Rodriguez, E., Gille, S. T., Cornuelle, B. D., Mazloff, M. R., Bourassa, M., Subramanian, A., van Sebille, E., Li, Q., Fox-Kemper, B., Ayet, A., Mouche, A., Merrifield, S. T., Terrill, E. J., Rio, M. H., Brandt, P., Farrar, J. T., Fewings, M., Chapron, B., Shutler, J. D., and Tsamados, M.: Integrated observations and modeling of winds, currents, and waves: requirements and challenges for the next decade, 6, 425, https://doi.org/10.3389/fmars.2019.00425, 2019.

Villas Bôas, A. B., Cornuelle, B. D., Mazloff, M. R., Gille, S. T., and Ardhuin, F.: Wave-Current Interactions at Meso and Submesoscales: Insights from Idealized Numerical Simulations, J. Phys. Oceanogr., in press, https://doi.org/10.1002/2016JC012413, 2020.

White, B. S. and Fornberg, B.: On the chance of freak waves at sea, J. Fluid Mech., 355, 113–138, 1998.

Appendix A: Ray equation in 1D

Let's consider a one dimensional stationary current shear: $\mathbf{u} = (\partial_x U x, 0)$ Starting from the ray equations in a Cartesian frame of coordinate (Mei, 1989; Phillips, 1977):

$$\partial_t k + \partial_x \omega = 0 \tag{A1}$$

ω is given by Eq. (2). The time derivative of the wavenumber k, assuming that intrinsic frequency constant:

$$\partial_t k = -k\partial_x U \tag{A2}$$

Which yield to:

$$2\partial_t \omega = -\omega\partial_x U \tag{A3}$$

As the wave action is conserved:

$$\frac{E(\sigma,\theta)}{\sigma} = Cte \tag{A4}$$

H_s is function of wave action (Eq. (3)), hence, wave height gradient (∇H_s) can be written:

$$\nabla(\frac{H_s}{\sigma}) = 0 \tag{A5}$$

400   Thanks to Eq. (A1) and knowing that $\partial_k \omega = C_g$, with C_g the wave train group velocity.

$$\nabla H_s \sim \frac{\partial_x U(H_s k)}{\sigma} \tag{A6}$$

Competing interests. Authors declare no conflict of interest in these works.

Author contributions. G.M designed the experiments, performed the numerical simulations and led the analysis of the results and writing. C.d.M provide the surface current fields used as the wave model forcing and contributed to the writing.

405   *Acknowledgements.* This work could not have been realized without the original idea proposed by Dr. Ana B. Villas Bôas, authors want to sincerely thank her. Also authors want to thanks their respective funders, G.M is supported both by the Centre National d'Etude Spatiale, focused on SWOT mission and the Region Bretagne through ARED program. C.d.M is funded by Direction Générale de l'Armement (DGA). Simulations were performed using the HPC facilities DATARMOR of "Pôle de Calcul Intensif pour la Mer" at Ifremer, Brest, France. We gratefully acknowledge B. Chapron for his helpful theoretical guidance. Finally authors acknowledge their respective Ph.D supervisors F.
410   Ardhuin and X. Carton for their thesis guidance all along the past few years.